Materials & Design 259 (2025) 114872

Contents lists available at ScienceDirect

Materials & Design

journal homepage: www.elsevier.com/locate/matdes

Generation of high-aspect-ratio 3C-SiC nanowires and evaluation of their potential as battery materials

Kanon Minami [a], Kentaro Shimazu [b], Yoshiyuki Hattori [b], Jiwang Yan [a,*]

[a] Department of Mechanical Engineering, Faculty of Science and Technology, Keio University, 3-14-1 Hiyoshi, Kohoku-ku, Yokohama 223-8522, Japan
[b] Division of Chemistry and Materials, Faculty of Textile Science and Technology, Shinshu University, Ueda, Nagano 386-8567, Japan

ARTICLE INFO

Keywords:
Silicon Carbide
Nanowire
Waste Silicon
Anode Material
Laser Irradiation

ABSTRACT

Waste Silicon (Si) powder generated during semiconductor manufacturing has attracted attention as a potential anode material for lithium-ion batteries. This study proposes a novel method to fabricate high-aspect-ratio cubic silicon carbide (3C-SiC) nanowires using a mixture of waste Si and graphite powders through laser processing. The mixture is placed between two plates to sandwich the laser-induced plume. This confinement promotes nanowire growth, increases the aspect ratio, shortens the lithium-ion diffusion length, and enables the fabrication of flexible electrodes. High-speed camera observations confirmed that the sandwiched plume was compressed and remained in air for nearly 10 s. Consequently, nanowires approximately 100–1200 nm in length and 15–60 nm in diameter (aspect ratio greater than 25) were generated. Electron diffraction and XRD analyses revealed that the nanostructures mainly comprised 3C-SiC. Battery performance evaluation tests of the generated nanowires showed that after 10 charge–discharge cycles at a current density of 50 mA/g, the SiC nanowires exhibited a specific capacity of 455 mAh/g, significantly higher than that of Si nanoparticles (291 mAh/g) and comparable to that of C-coated SiC nanoparticles (477 mAh/g). The SiC nanowires outperformed both Si nanoparticles and graphite anodes, demonstrating the potential of the proposed method in next-generation lithium-ion battery (LIB) anode fabrication.

1. Introduction

With the advancement of the semiconductor industry, large quantities of Si powder are generated as by-products during the fabrication of semiconductor chips. For example, approximately 50 % of the raw Si is removed from Si ingots during the wafering process, and furthermore, approximately 90 % of the raw Si is removed from the wafers during the process of back side grinding. Currently, the Si powder is disposed of as waste, resulting in significant resource loss. Consequently, developing effective Si waste recycling technologies has become crucial. In recent years, with the increasing global emphasis on sustainable manufacturing and circular economies, technologies that convert industrial waste into high-value-added materials have become essential to reduce environmental impacts and improve management of limited resources.

Research on the effective utilization of waste Si powder, particularly as an anode material in lithium-ion batteries (LIBs), has gained significant attention [1,2]. Owing to its high theoretical capacity of approximately 4200 mAh/g, Si is regarded as a highly promising next-generation anode material, far outperforming conventional graphite-based materials. However, during charge–discharge cycles, Si undergoes volumetric expansion exceeding 300 %; this causes particle pulverization, interfacial degradation, and electrode structure collapse [3], ultimately resulting in rapid capacity fading. To address these challenges, two main strategies have been proposed: the nanosizing of Si [4,5] and formation of Si–carbon (Si/C) composites [2]. Chan et al. reported that Si nanowires exhibit strong resistance to pulverization during cycling and maintain excellent electrochemical performance [4]. Sourice et al. [5] and Qi et al. [6] demonstrated that Si@C core–shell nanoparticles, consisting of Si nanoparticles coated with carbon, offer both high and stable capacities. Li et al. explored generating Si nanowires from waste Si powder and depositing them onto carbon cloth for a kind of SiNWs@CC composite material and further demonstrated their usefulness as an anode material [7].

In addition to Si/C composites, silicon carbide (SiC) materials have attracted attention as a means of preventing electrode degradation. SiC is known for its high mechanical strength, chemical stability, and excellent thermal conductivity and has traditionally been used in power and harsh-environment devices. Although SiC is considered unsuitable

* Corresponding author.
E-mail address: yan@mech.keio.ac.jp (J. Yan).

https://doi.org/10.1016/j.matdes.2025.114872
Received 5 August 2025; Received in revised form 30 September 2025; Accepted 30 September 2025
Available online 1 October 2025

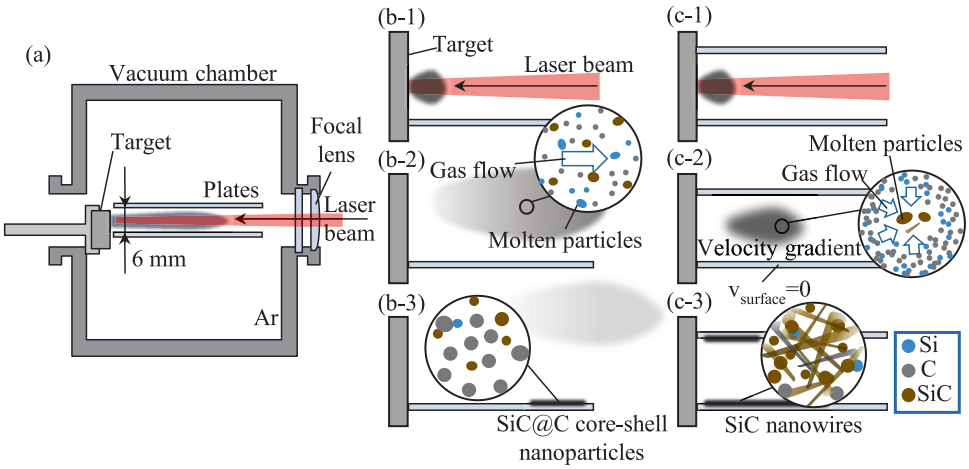

Fig. 1. Method of confinement using two slide glasses: (a) Schematic diagram of irradiation, (b) Plume behavior without confinement, (c) Plume behavior with confinement.

as an anode material owing to its chemical inertness toward lithiation [8], nanostructured SiC materials exhibit promising electrochemical properties. For example, 3C-SiC nanoparticles [9] and 4H-SiC nanocrystalline SiC thin films [10] have shown good charge–discharge performance, indicating that nanosizing is also an effective approach for SiC. Chen et al. revealed that although bulk SiC is inactive toward lithiation, the introduction of Si vacancies or boron doping can activate it [11]. Wang et al. reported that nitrogen-doped 3C-SiC nanoparticles exhibited good capacity retention [12], and Shtepliuk et al. proposed that 4H-SiC substrates coated with graphite layers could serve as potential anode materials [13]. Li et al. demonstrated that ultrathin bowl-shaped SiC nanoshells encapsulated in hollow graphite-like carbon spheres (SiC@HGS) exhibit excellent capacity retention and rate performance [14]. These studies suggest that with a proper design, SiC has great potential as a battery material.

When using waste Si powder as a raw material for battery electrodes, the waste Si may contain metallic or nonmetallic impurities, necessitating a process such as acid cleaning to remove them[15,16]. For grinding silicon waste, the presence of abrasive particles like diamond or silicon carbide is a common issue: Momoki et al. reported that laser irradiation in air can sublimate the carbon sources of such abrasives, which then react with atmospheric oxygen to form CO_2, effectively removing them [17]. Minami et al. reported the formation of SiC@C core–shell nanoparticles [18] and multilayer graphene-coated SiC nanowires [19] by irradiating a mixture of waste Si powder and graphite powder with a laser. Carbon from sublimated abrasives, such as diamond and SiC, and graphite react with Si sources to form SiC. Laser-based synthesis of SiC nanomaterials does not require complex preprocessing, hazardous chemicals, or catalysts, making it a simple and environmentally friendly process. Moreover, laser irradiation offers noncontact, localized, and rapid heating, allowing for shortened reaction times and precise control in nanostructure formation.

However, nanowires obtained using previously reported laser irradiation methods had limited growth [20], with aspect ratios rarely exceeding 20, and the low yields made it difficult to collect sufficient quantities for battery evaluation [19]. Furthermore, previous studies on laser irradiation of waste Si powder focused on the morphology and formation mechanisms of the resulting SiC-based nanostructures [18,19]; their electrochemical performance as LIB anode materials has not been sufficiently evaluated, limiting their applicability in real devices.

In this study, a novel process to fabricate high-aspect-ratio nanowires is proposed. A plasma plume generated by laser irradiation is confined between two plates. This confinement suppresses the expansion of the plume into the surrounding atmosphere, enabling efficient nanowire collection. Previous studies attempted to improve the detection sensitivity of laser-induced breakdown spectroscopy (LIBS) by increasing the plasma density through the confinement of laser-induced plumes. In these studies, plasma confinement and compression were investigated using two plates, primarily in combination with nanosecond-pulse lasers with a plate spacing of less than 10 mm [21–24]. Laser-induced plumes and shock waves were generated under nanosecond pulse laser irradiation. These shock waves get reflected between the plates, thereby compressing the plume and leading to increased plasma temperatures and electron densities owing to spatial confinement [24]. In such studies, plume compression were observed approximately 10 microseconds after shockwave generation. To the best of our knowledge, the confinement effects of plumes generated by millisecond pulses have not yet been reported. Owing to the distinct timescales involved, millisecond pulse lasers do not exhibit the same rapid energy deposition as nanosecond pulses, making it unclear whether a similar shockwave-mediated compression occurs. However, fluidic confinement effects between the parallel plates are still expected. The plume velocity has shown to be a key parameter influencing the aspect ratio of resulting nanostructures. When the plume was confined between the two plates, its interaction with the ambient gas reduced, thereby maintaining a high-temperature state; this promoted nanowire growth and significantly enhanced the aspect ratio. Enhancing the aspect ratio increases the electron transport distance per nanowire and improves the interconnectivity within the electrode, while shortening the lithium-ion diffusion path [25]. These features may contribute to the improved performance of flexible electrodes and enhance the applicability of the material to non-battery uses, such as in bioelectrodes [26,27]. Furthermore, LIB half-cells were fabricated using the synthesized materials and 10-cycle charge–discharge tests were conducted to evaluate their initial electrochemical properties. The results indicate an important step toward the practical application of waste Si-derived SiC-based nanomaterials.

2. Experimental procedure

2.1. Preparation of Si/C mixture target

Waste Si powder was generated in both stages of the silicon wafer manufacturing process: rough grinding with a resin-bonded diamond wheel and fine grinding with a vitrified bonded diamond wheel. The average particle diameter of the waste Si powder thus obtained was 3.9 μm. It was mixed with 50-μm grain size graphite powder (Kojundo Chemical Laboratory Co., Ltd., Japan) in a ratio of 1:2 (wt%) and milled for 3 h in a pot milling machine. After treatment, the Si and C particle

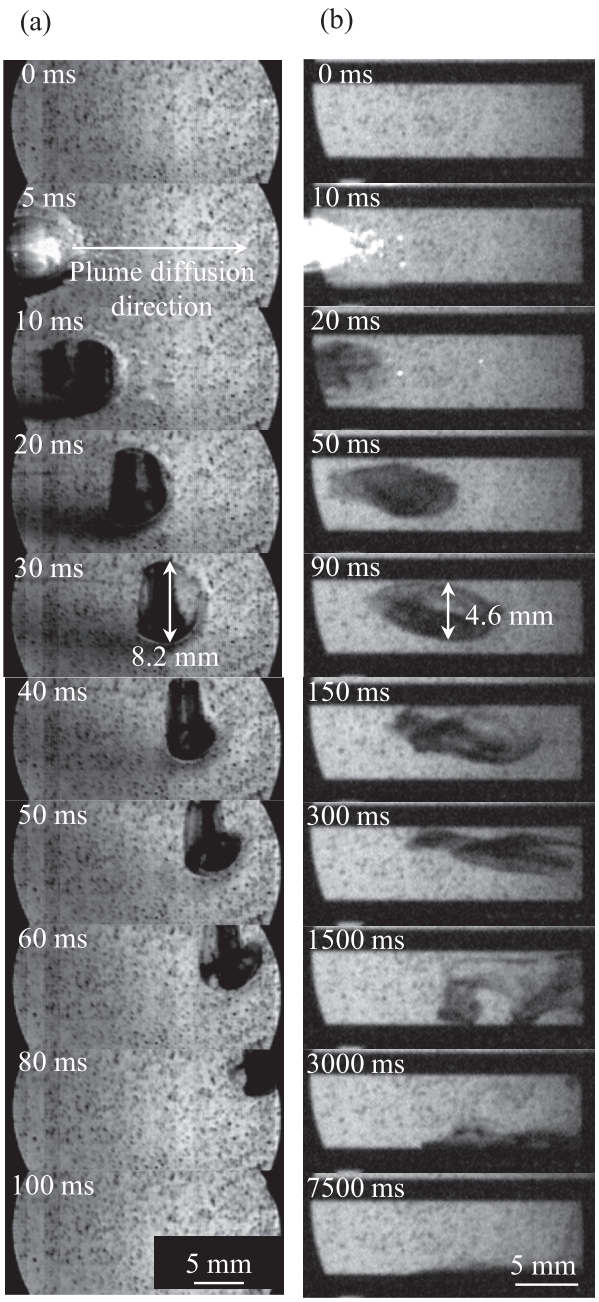

Fig. 2. Schlieren images of two conditions: (a) with no plate above or below the plume, (b) with two plates between the top and bottom of the plume.

sizes were reduced to approximately 1 μm and 20 μm, respectively. The waste Si powder used in this study had a purity of approximately 99 %. However, it is conceivable that some collection systems might generate lower-purity waste Si powder. Since SiC and diamond abrasive grains act as carbon sources within the laser-induced plume, as necessary it would be possible to adjust the optimal graphite mixing ratio depending on the concentration of these grains. Finally, a cylindrical target with 10-mm diameter and 10-mm height was produced by applying a 40 kN load for 1 min using a tablet-type compression molding machine.

2.2. Plume-confinement laser irradiation for nanowire formation

To increase the yield of nanostructures generated by a single laser pulse, we employed millisecond pulses from a high-energy continuous-wave (CW) laser for material synthesis. Minami et al. demonstrated that

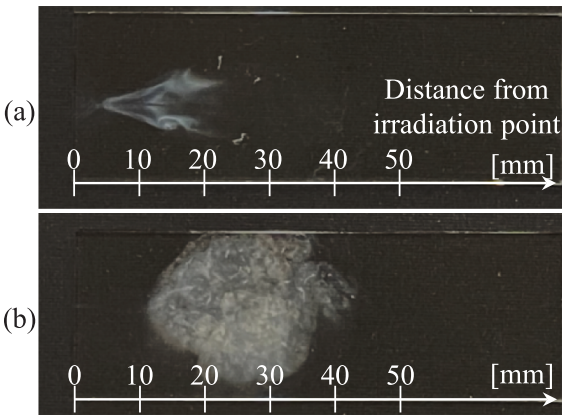

Fig. 3. Image of the deposition on (a) the upper and (b) lower plates after five irradiations.

when a mixed target of Si and graphite powders was irradiated with a 10 ms laser pulse under focused conditions, nanoparticles were formed; when the laser was defocused, nanowires were produced. With the increasing degree of defocusing, the aspect ratio of the nanowires also increases [19]. However, the amount of material ablated from the target and ejected as plume decreases, resulting in a lower yield of nanostructures. This indicates a trade-off between the nanowire aspect ratio and production yield. To simultaneously improve the number of nanowires produced per pulse and their aspect ratio, the laser-induced plume was confined using two plates.

Fig. 1 shows a schematic of the confinement method using two plates. As shown in Fig. 1 (a), the target and two plates were placed inside the chamber. Four blocks (6 mm in height, 5 mm in width, and 10 mm in depth) were positioned at the ends of the plates to maintain a parallel alignment between the upper and lower plates. Laser irradiation was conducted in a chamber filled with Ar gas at 0.1 MPa. A single-mode continuous-wave ytterbium (Yb) fiber laser with a Gaussian beam distribution (YLR-500-AC, IPG Photonics Co., USA) operating at a wavelength of 1070 nm and an output power of 390 W was focused using a lens with a focal length of 200 mm. The target was laterally displaced 28 mm from the focal point to achieve defocused irradiation. The laser beam was directed into the space between the plates. A pulse generator was used to produce single laser pulses with a pulse width of 10 ms. To evaluate the effect of plume confinement by the two plates, additional experiments were performed under reference conditions in which only one plate was placed 5 mm below the target.

Fig. 1(b,c) schematically illustrates the proposed mechanism for nanowire formation. When the Si/C mixed target was laser irradiated (Fig. 1(b-1, c-1)), a laser-induced plume was generated. In the absence of confinement, the plume expanded freely without obstruction (Fig. 1(b-2)). During this process, a small fraction of the plume cooled down, and nanostructures were deposited on the lower plate (Fig. 1(b-3)).

On the contrary, when the plume was passed between two plates, a confinement effect occurred. Ideally, the fluid velocity at the wall surfaces is zero; however; the viscous drag near the plate surfaces induced a velocity gradient within the plasma. This suppressed the spatial expansion of the plume and caused partial compression compared with the unconfined case (Fig. 1(c-2)). The increased plume density enhanced the precursor supply and promoted the nanowire formation. Further, the plume decelerated, leading to reduced scattering and more effective deposition on the plate surfaces (Fig. 1(c-3)).

In this study, nanowires were synthesized in a catalyst-free environment. It is assumed that the nanowire growth occurs via a self-catalyzed vapor–liquid–solid (VLS) mechanism [28,29] involving the diffusion of gas into molten SiC or Si nanoparticles [30] or via a vapor–solid (VS) mechanism [31–33]. In both mechanisms, continuous vapor-phase precursor supply [33] and sustained high-temperature

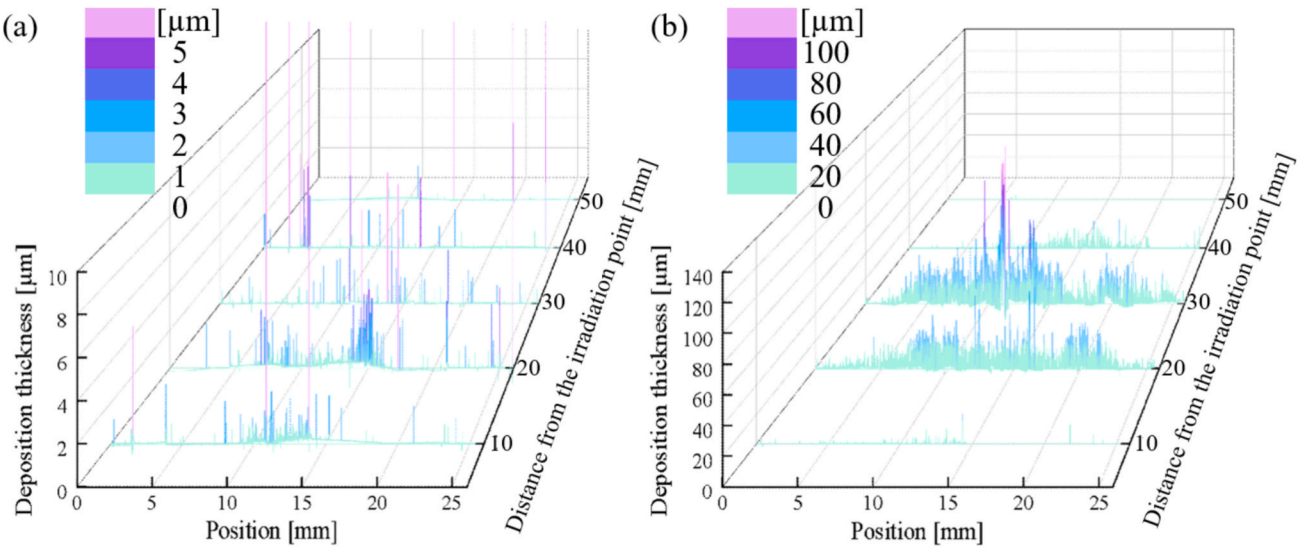

Fig. 4. Cross-sectional profile showing the amount of deposition on (a) the upper and (b) lower plates after 10 irradiations.

conditions [34,35] are essential for nanowire growth. Plume confinement is expected to increase the plume density and help maintain elevated temperatures, thus facilitating these conditions.

2.3. High-speed camera observation of plume

The laser-induced plumes were photographed to confirm the differences between the two plates. A high-speed camera (FASTCAM Mini AX50; Photron Ltd., Tokyo, Japan) was used to capture images of the plumes. Two plume generation conditions were captured—a plume generated with two sandwiched plates and a plume generated by laser irradiation without the plates installed. Further, the differences in the plume shape and residence time with and without the use of the two plates were observed. The Schlieren method was used for imaging. This is because, in normal imaging mode, although the shape of the plume during laser irradiation can be clearly captured, the plume becomes dark after laser emission is completed, and the complete process of plume propagation cannot be observed. The Schlieren method is a technique for visualizing density gradients. To obtain a Schlieren image, a collimating lens and a point light source are used to create parallel beams of light through which a plume is passed. The plume disturbs and refracts parallel rays. The rays emitted through a pinhole positioned at the focus of the lens depend on the refractive index of the medium rays in the measurement area, allowing the density gradient to be visualized. This method is ideal for observing the behavior of the plume after laser emission has ended.

2.4. Deposition morphology and composition analysis of nanostructures

To determine the thickness distribution of the nanostructures deposited on the two plates, cross-sectional profiles were measured using a laser microscope (LEXT OLS4100, OLYMPUS Ltd., Japan). The weights of the plates before and after irradiation were measured using an electronic balance (XSE105, Mettler Toledo Company, Switzerland) with a least count of 0.01 mg, and the difference was calculated to determine the amount of deposition. To obtain reliable results for the amount of deposition in these measurements, nanostructures were deposited on the same plate after five single-shot irradiations at different locations from the previous irradiation position by rotating the target at sufficient time intervals. To obtain the nanostructures on the same plate, the target was rotated. The nanostructures on the plates were observed by scanning electron microscopy (SEM, Inspect F50, FEI Company, USA) and transmission electron microscopy (TEM, Tecnai G2, Technai Osiris, FEI Company, USA). The composition of the nanoparticles was assessed by TEM, and mapping analysis was performed using Energy-dispersive X-ray spectroscopy (EDX) and X-ray Diffraction (XRD, D8 Discover, BRUKER Ltd., USA) analysis. For the XRD analysis, measurements were performed using a 1 mm divergence slit to irradiate the sample with an X-ray beam. Deposits were collected five times to gather a sufficient amount for the measurement in the XRD analysis.

2.5. Battery performance evaluation test of SiC nanowire, C-coated SiC nanoparticle, and Si nanoparticle electrode

The electrodes were prepared using the generated SiC nanowires. The generated SiC nanowires were combined with carbon black and polyvinylidene fluoride at a volume ratio of 1:10:1 and milled. N-Methylpyrrolidone was then added, and the mixture was made into a slurry. The slurry was dried at 30 °C for 12 h and subsequently vacuum-dried at 110 °C for 24 h to prepare a 10-mm diameter electrode. Using the same method, an electrode with only C-coated SiC (C/SiC) nanoparticles ranging from less than 10 nm to 40 nm in diameter and an electrode with only Si nanoparticles ranging from 10–20 nm in diameter were prepared for comparison.

In the constant-current charge–discharge measurements, the counter electrode was made of Li metal, and the working electrode was made of the fabricated electrode. The electrolyte was a mixture of 1 mol/L lithium hexafluorophosphate (LiPF6), ethylene carbonate (EC), and diethyl carbonate (DEC) at a volume ratio of 1:1. A two-electrode cell and a current density of 50 mA/g were used. Charge–discharge cycles were repeated ten times, and the reversible capacity and cycling performance were determined. As our material synthesis was based on single-shot ablation to explore the dynamics of plume confinement effect, the quantity of nanostructures produced was insufficient for long-term cycling performance tests that typically span hundreds of cycles. To demonstrate the fundamental viability of the synthesized material, we performed a preliminary, laboratory-scale battery evaluation for ten cycles. As demonstrated in previous studies [36], the first several cycles were usable to assess the initial charge–discharge behavior and to establish the potential of the material. In this study, the cycling performance was evaluated based on coulombic efficiency and capacity retention. To assess the high-rate capability, charge–discharge tests were conducted at current densities of 50, 100, 500, and 1000 mA/g. Although the nominal current densities were identical for all the three types of working electrodes, deviations between the set and actual current values were observed for the nanowire and C/SiC particle

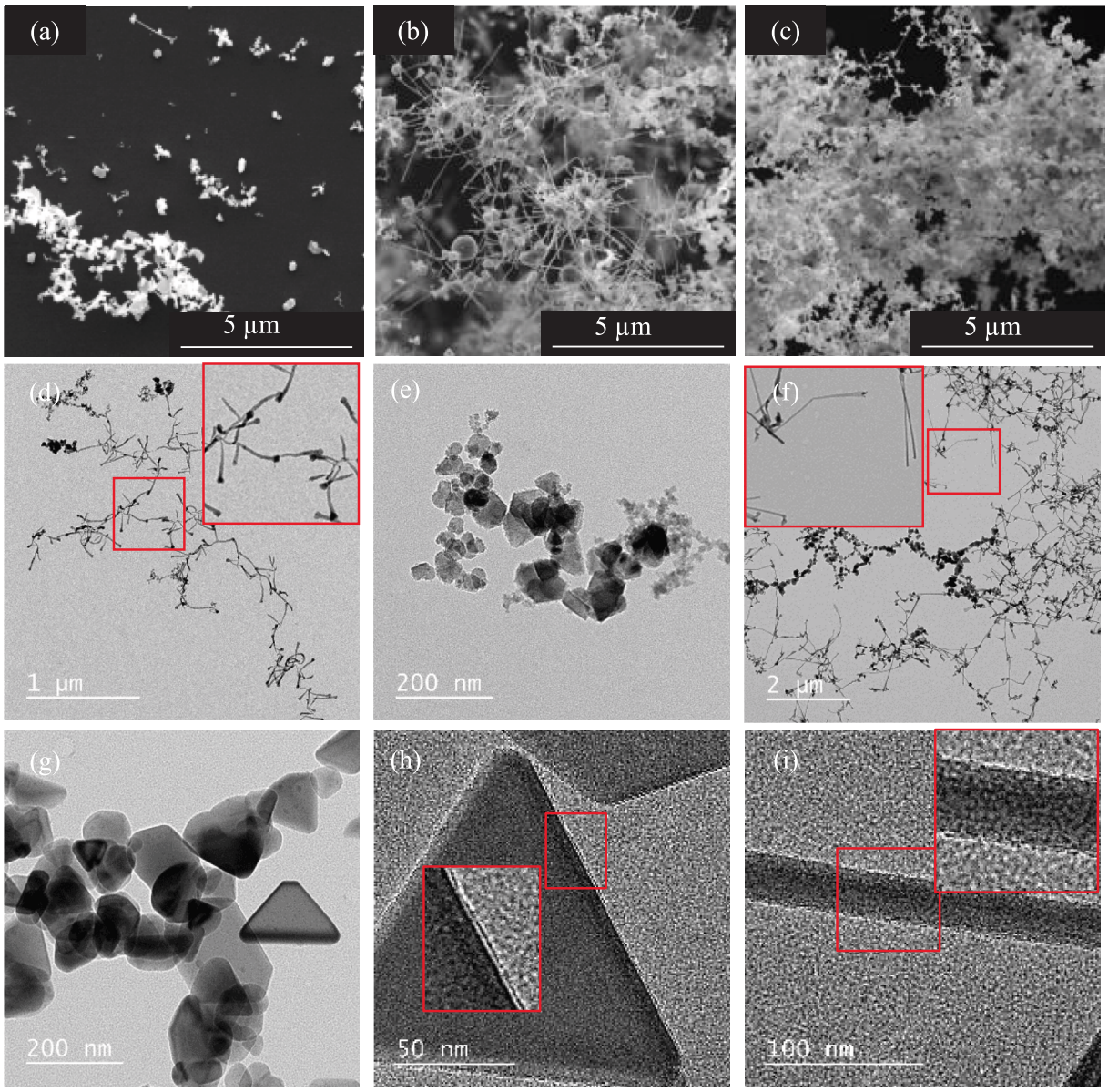

Fig. 5. SEM images of nanostructures deposited on (a) the upper and (b), (c) lower plates; TEM images of nanostructures deposited on (d), (e) the upper and (f), (g), (h), (i) lower plates.

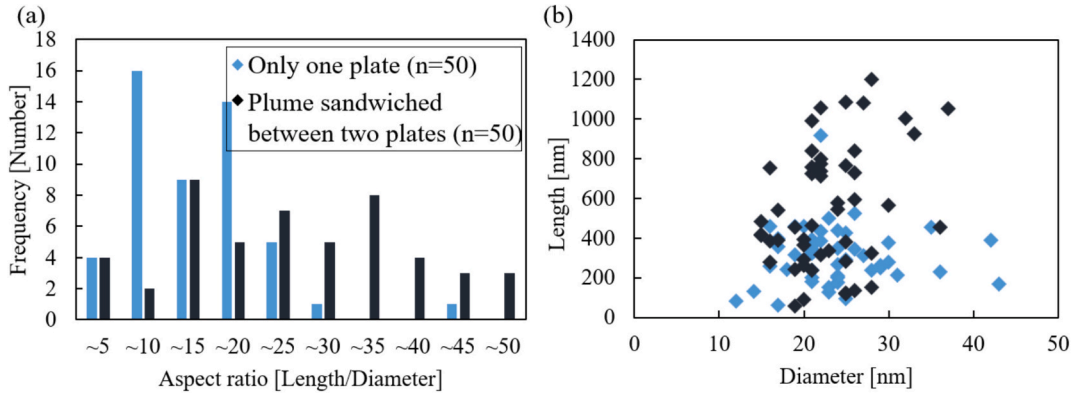

Fig. 6. Distribution of aspect ratios of nanowires produced in an environment with only one plate and (b) nanowires produced in an environment sandwiched between two plates.

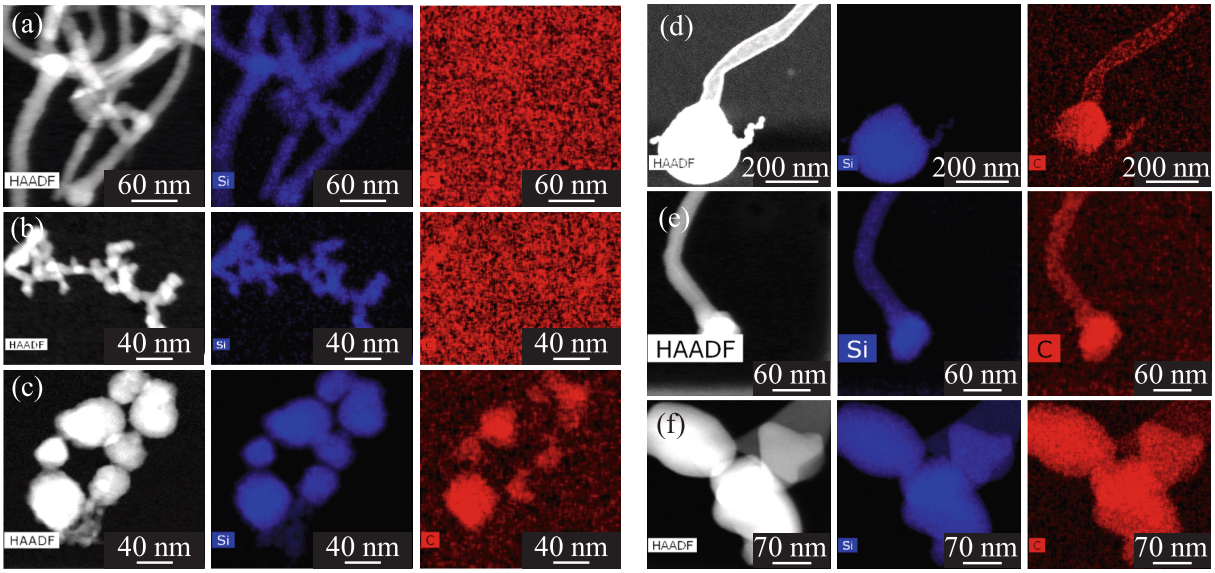

Fig. 7. EDX mapping analysis of (a) nanowires and (b)(c) nanoparticles deposited on the upper plate; (d),(e) nanowires and (f) nanoparticles deposited on the lower plates.

samples. In contrast, the measured current in the Si-nanoparticle electrode closely matched the nominal applied current density. When current densities were set at 50, 100, 500, and 1000 mA/g, the measured values were 100, 153, 550, and 1055 mA/g for the SiC nanowires electrode and 67, 133, 522 and 1033 mA/g for the C-coated SiC core–shell nanoparticles electrode, respectively.

3. Results and discussion

3.1. In-situ plume observations

Observations of the plume in the Schlieren mode of the high-speed camera are shown in Fig. 2. In the absence of the plate (Fig. 2(a)), the plume continued to expand even after the end of irradiation, and the plume widened to 8.2 mm after 30 ms from the start of irradiation (20 ms after the end of irradiation). In contrast, when the plume was sandwiched between plates (Fig. 2(b)), the plume remained in air with a small width of approximately 4.6 mm for a considerably long time after irradiation. In addition to the plume width, there was a significant difference in the speed at which the plume extended. Without the plates, the plume diffused diagonally upward and left the field for approximately 100 ms, as shown in Fig. 2(a). The plume between the plates remained in the same location for a very long time, as shown in Fig. 2(b), and it took nearly 1 s for the plume to start depositing. Complete deposition took approximately 10 s. By sandwiching the plume between plates, the scattering distance of the plume could be limited, and the nanostructures generated in the plume could be deposited and collected efficiently.

The shape of the plume shown in Fig. 2 is similar to that of the compression plume identified in a previous study using nanosecond pulsed lasers [21], suggesting that even millisecond pulses had sufficient compression effects between parallel plates.

3.2. Amount and morphology of nanostructure deposits

The deposits on the two plates after five irradiations are shown in Fig. 3. On the upper plate (Fig. 3(a)), a thin, long, and very small deposit was observed at 0–20 mm from the target. On the lower plate (Fig. 3(b)), thicker deposits were observed at approximately 10–40 mm from the target. The cross-sectional profiles of the plates are shown in Fig. 4. The deposition on the upper plate (Fig. 4(a)) was only a few micrometers, indicating that the deposition was concentrated at the center of the plate. On the contrary, on the lower plate (Fig. 4(b)), depositions were more frequent at distances of 20 mm and 30 mm from the target, with the thickest deposition at a distance of 30 mm from the target exceeding 100 μm. Deposition was rarely observed at distances greater than 50 mm from the target. The weight of the deposits on the lower plate was approximately 0.20 mg all five times, while the deposits on the upper plate were so small that they could not be detected on the electronic scale. Under the condition where deposition occurred on only one plate, the deposited amount was measured to be 0.08 mg after five irradiations. This clearly shows that more than double the amount can be obtained by confining the plume. The SEM and TEM images of the deposits on the upper and lower plates are shown in Fig. 5. Fig. 5(a–c) shows that both nanoparticles and nanowires were produced on both plates, although there were significant differences in the amounts produced. Compared to the nanostructures deposited on the lower plate (Fig. 5(a)), the amount of material deposited on the upper plate was significantly less (Fig. 5(b, c)). It is believed that these were particles scattered from the plume during the early stages of ejection. While the deposits on the lower substrate had more time to float and grow into nanowires, the deposits on the upper substrate, which were scattered and deposited early, consisted almost entirely of nanoparticles with very few nanowires.

The high magnification TEM images shown in Fig. 5(d–g) indicate that the nanowires deposited on the upper plate (Fig. 5 (d, e)) are 100–400 nm long with a diameter of 10–20 nm, and the particle size of the produced nanoparticles is 10–70 nm; the length of the nanowires on the lower plate (Fig. 5(f, g)) is 100–1200 nm with a diameter of 15–60 nm, and the particle size of the produced nanoparticles is 50–200 nm. TEM images of the surfaces of the nanoparticles and nanowires are shown in Fig. 5(h, i). Some graphite films can be clearly observed on the surface (Fig. 5(h)), whereas others were very slight or indistinct (Fig. 5 (i)). Although graphite layers were formed on some nanoparticles and nanowires, they were incomplete.

The plume confinement effect of the two plates was compared with that of the condition in which only one plate was placed 5 mm under the target. The lengths and diameters of 50 nanowires for each condition were measured from the TEM images, and the aspect ratio frequencies are shown in Fig. 6. When the plume was sandwiched between two plates, 48 % of the nanowires had lengths greater than 500 nm, and when only one plate was placed at the bottom of the plume, only 4 % of

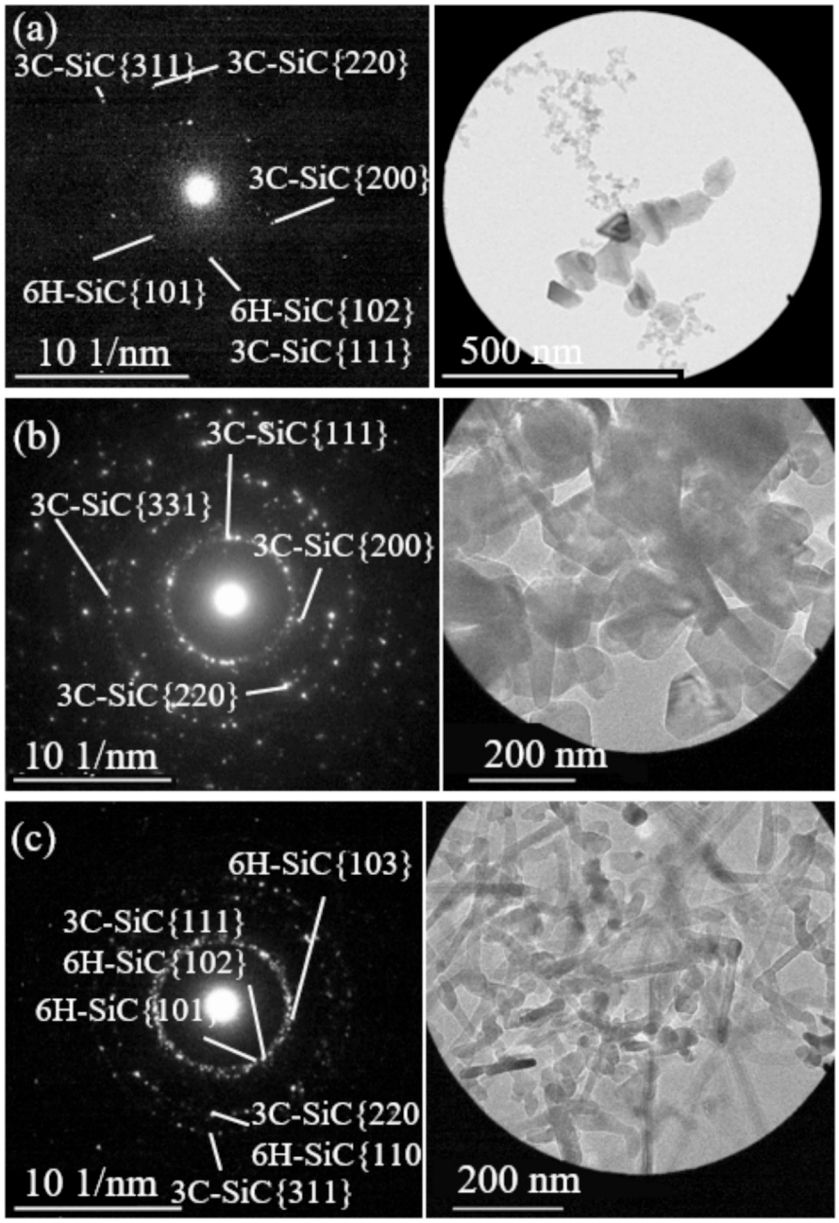

Fig. 8. SAED pattern of nanomaterials: (a) nanoparticles deposited on the upper plate, (b) nanoparticles, and (c) nanowires deposited on the lower plate.

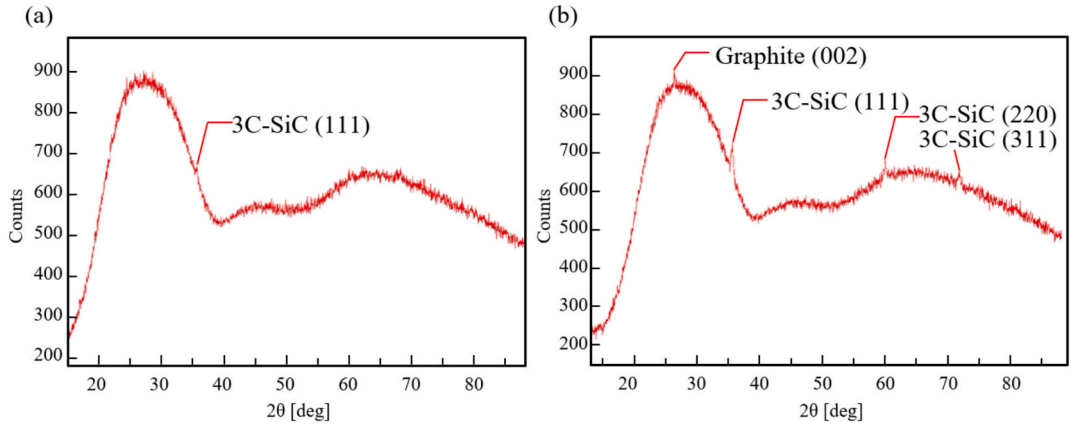

Fig. 9. XRD analysis of nanomaterials on (a) the upper and on (b) lower plates.

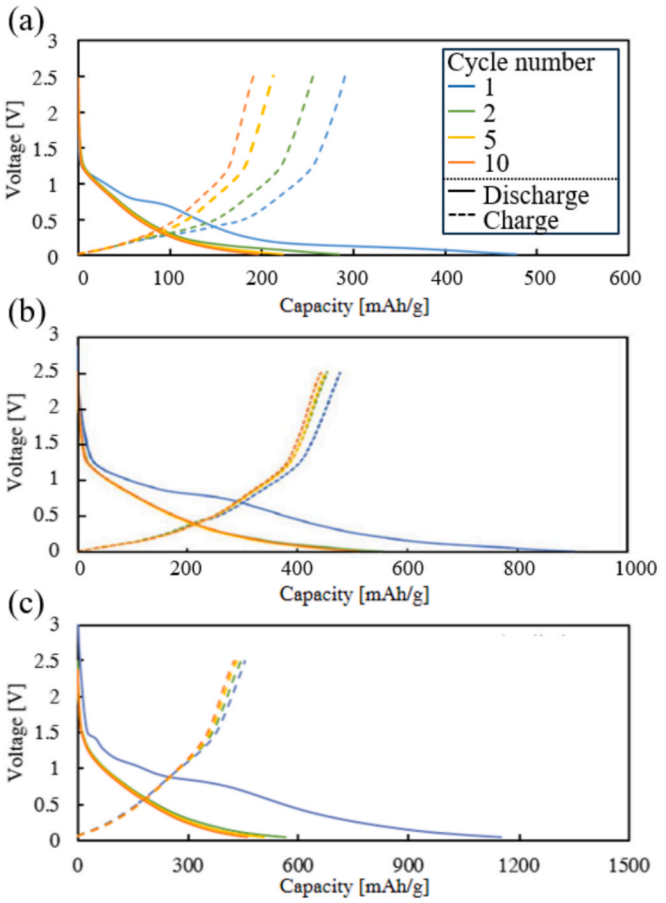

Fig. 10. Results of constant-current charge–discharge measurements of (a) anode with Si nanoparticles, (b) anode with C-coated SiC nanoparticles, and (c) anode with SiC nanowires.

the nanowires had lengths greater than 500 nm. Nanowires with an aspect ratio greater than 25 were present in 46 % of the cases where the plume was sandwiched between two plates and in 4 % of the cases where only one plate was placed at the bottom of the plume.

3.3. Compositional analysis

In Fig. 7, the EDX mapping analysis of deposits on the upper (Fig. 7 (a–c)) and lower (Fig. 7 (d–f)) plates is presented, with Si and C marked in red and blue, respectively. Fig. 7(a,b) shows that nanowires and fine nanoparticles consisted of only Si, whereas Fig. 7(c) shows that larger nanoparticles consisted of both Si and C. As shown in Fig. 7(d), there is no presence of Si in the nanowire and only C is observed. This suggests that nanowires consisting of only C were generated. However, almost all the deposited nanowires and particles consisted of both Si and C, as shown in Figs. 7(e) and (f).

The electron diffraction results from TEM observations are shown in Fig. 8. Figs. 8(a) and (b) show the upper and lower plates, respectively. As shown in these figures, 3C-SiC and 6H-SiC were detected on both plates. The XRD results for the upper and lower plates are shown in Fig. 9. In addition to the large broad peaks indicating the presence of both plates, 3C-SiC peaks were detected on the upper plate (Fig. 9(a)), and 3C-SiC and graphite peaks were detected on the lower plate (Fig. 9 (b)). Because of the limited number of deposited particles, the peaks on both plates were small. The XRD analysis, which provides an overview of the entire deposition of nanostructures, confirms that 3C-SiC is the main product. In contrast, the TEM electron diffraction analysis is a highly localized technique, focusing on specific areas of just a few hundred nanometers. Thus, while 6H-SiC is not present in sufficient

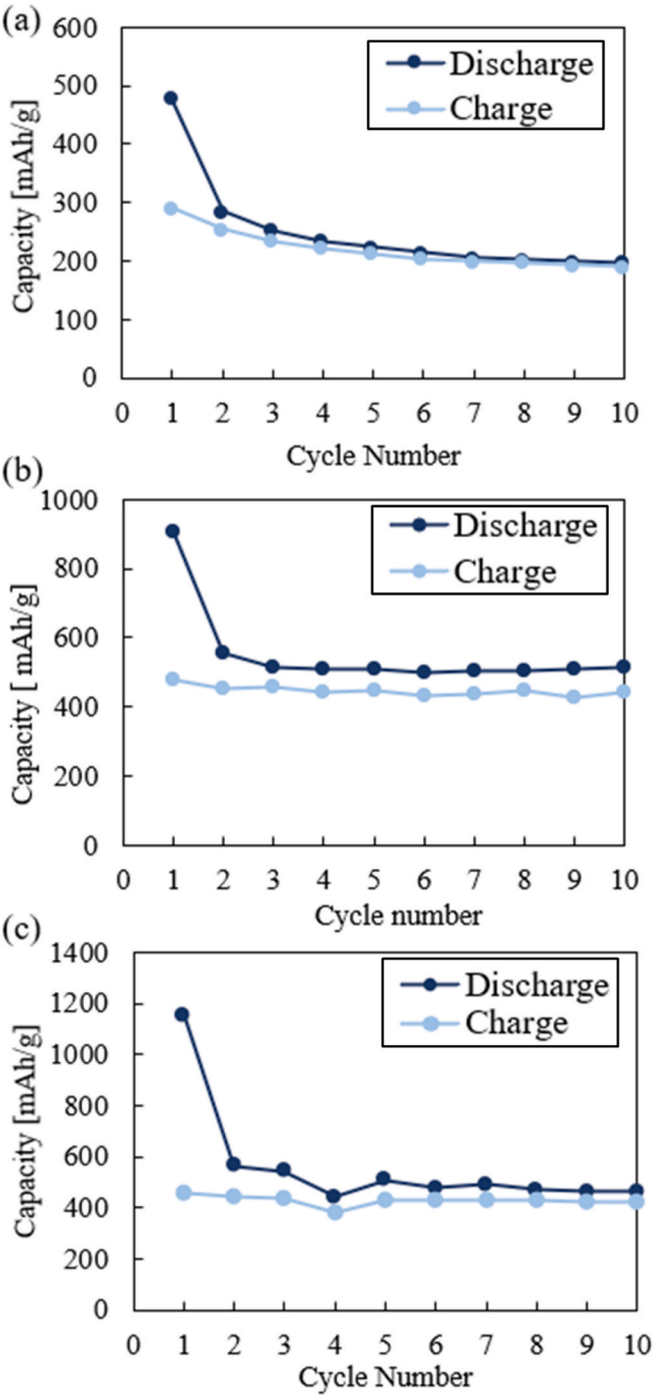

Fig. 11. Ten-cycle charge–discharge graphs of (a) anode with Si nanoparticles, (b) anode with C-coated SiC nanoparticles, and (c) anode with SiC nanowires.

quantities to be detected as a major product by XRD, the TEM results suggest that a very small amount is mixed in with the dominant 3C-SiC. From these results, it can be concluded that the main product is 3C-SiC. The EDX mapping analysis and electron diffraction results also indicate that Si, C, and 6H-SiC may be mixed in very small quantities.

3.4. Battery electrode performance evaluation

To verify the performance of SiC nanowires as a lithium-ion battery electrode material, battery evaluation tests were carried out using an electrode with the generated SiC nanowires, Si nanoparticles, and C/SiC nanoparticles, respectively. Although the products in this study include

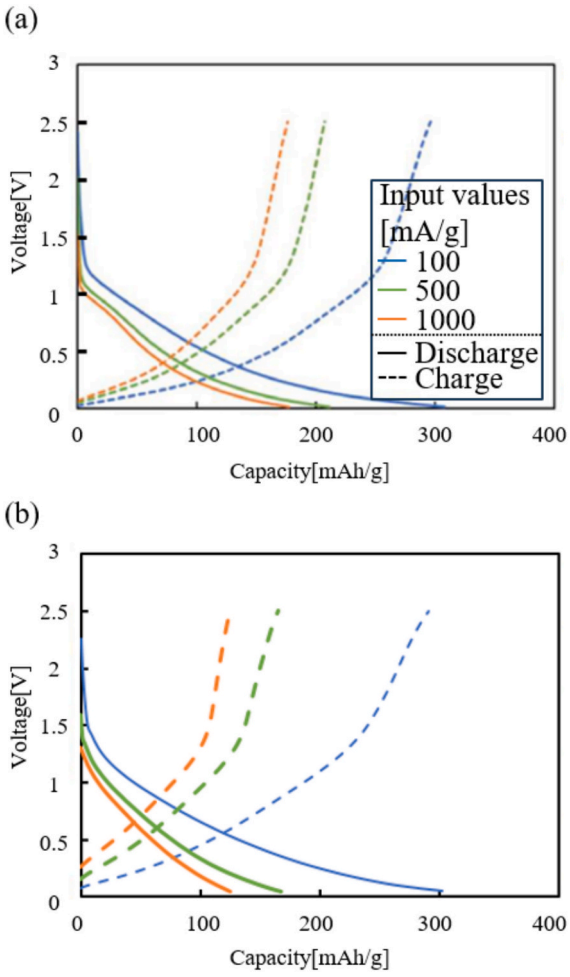

Fig. 12. Rapid charge–discharge tests (input values of 100 mA/g, 500 mA/g and 1000 mA/g) of (a) anode with C-coated SiC nanoparticles and (b) anode with SiC nanowires.

both SiC nanowires and nanoparticles, the electrode is hereafter described as 'electrode with SiC nanowires' to distinguish it from the electrode containing only SiC nanoparticles.

The results of the constant-current charge–discharge measurements at a current density of 50 mA/g are shown in Fig. 10. The large irreversible capacitance observed during the first discharge was due to the formation of a solid electrolyte interphase (SEI) layer. During the first charge, the reversible capacities were 291, 477, and 455 mAh/g for the electrode of Si nanoparticles, SiC nanoparticles, and SiC nanowires, respectively. The theoretical capacity of graphite—which is currently widely used as an electrode material in lithium-ion batteries—is 370 mAh/g; here, a reversible capacity exceeding that of graphite was achieved.

It also exhibited a higher reversible capacity than Si, which is known to have almost ten times the theoretical capacity of graphite. The discrepancy between the experimental capacity of the Si-based electrodes and the theoretical capacity of Si is likely due to the high proportion of carbon black used in our formulation. In a previous study, a half-cell assembled with only carbon black and PVDF demonstrated a specific capacity of just 2 mAh/g during a constant-current charge–discharge test at 50 mA/g [37]. Fig. 11 shows the evolution of the capacity of each electrode after 10 cycles repeated at a current density of 50 mA/g. The capacity retention rate, which is the charge capacity at the tenth cycle divided by the charge capacity in the first cycle, was 65.7 %, 92.6 %, and 93.6 % for the electrode with Si nanoparticles, SiC nanoparticles, and SiC nanowires, respectively. Compared to Si

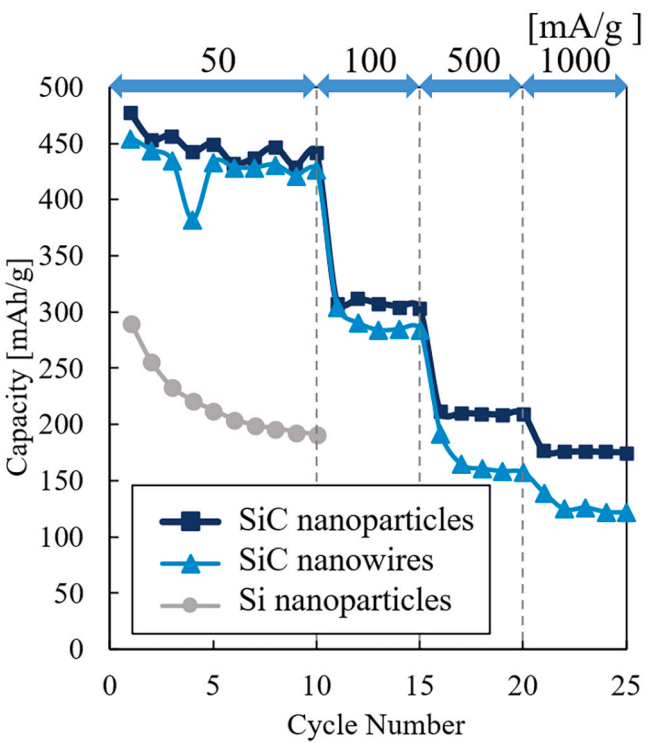

Fig. 13. Comparison of rate characteristics of anode with Si nanoparticles, anode with C-coated SiC core–shell nanoparticles, and anode with SiC nanowires.

nanoparticles, SiC nanostructures are considered less likely to break down the crystal structure of the active material during charging and discharging and to drop out of the current collector.

The Coulombic efficiency, calculated by dividing the charge capacity by the discharge capacity, was approximately 90 % for electrodes with Si nanoparticles, SiC nanoparticles, and SiC nanowires. These results show that the SiC nanostructures have a very stable cycling performance, with good capacity retention and Coulombic efficiency.

The results of charging and discharging at high current densities using the electrodes with each SiC nanostructure are shown in Fig. 12. The charge and discharge capacities of the SiC-nanoparticle electrodes at 100, 500, and 1000 mA/g were 296, 207, and 176 mAh/g, respectively. For the SiC nanowire electrode, the charge–discharge capacities at 100, 500, and 1000 mA/g were 291, 165, and 125 mAh/g, respectively.

A graph comparing the rate characteristics of electrodes with Si nanoparticles, SiC nanoparticles, and SiC nanowires is shown in Fig. 13. The electrode with SiC nanoparticles and SiC nanowires showed a stable charge–discharge capacity at higher densities, indicating its potential for rapid charge–discharge.

Comparing SiC nanoparticles and SiC nanowires, the SiC nanoparticles exhibited a slightly higher performance. The insufficient graphite coating on the surface of the SiC nanowires and the lack of alignment of the SiC nanowires are considered the primary causes of this difference.

Efficient electron transport from the current collector to the nanowires is necessary to improve the battery performance [4]. If nanowires with a high aspect ratio are aligned in the same direction, the diffusion length of the Li ions can be shortened [25]. Increasing the density of the nanowires and enhancing the alignment of their orientation would enable their use as high-performance battery materials that are resistant to fast charging/discharging and electrode strain.

4. Conclusions

This study demonstrated a simple and effective laser-based method for synthesizing high-aspect-ratio SiC nanowires from waste Si powder. By confining the laser-induced plume between the two plates, the nanowire morphology and production efficiency were both improved. Key findings include:

(1) Plume confinement was confirmed via high-speed camera imaging, which showed suppressed expansion and extended residence time when the plume was sandwiched between the plates.
(2) 3C-SiC nanowires were successfully formed, with lengths of 100–1200 nm and diameters of 15–60 nm, as confirming by TEM observation of the deposited materials.
(3) Plume confinement promoted nanowire growth, likely attributed to the increased plume density that enhanced the Si–C reactions and the sustained high-temperature environment that supported the continued growth.
(4) Battery performance tests showed that SiC nanowires delivered a specific capacity of 455 mAh/g after 10 charge–discharge cycles at a current density of 50 mA/g outperforming Si nanoparticles under the same conditions.
(5) The C-coated SiC nanoparticles exhibited a better performance than the nanowires under high-rate cycling, suggesting future improvements through surface coating and nanowire alignment.

These results demonstrate that a simple two-plate confinement setup enables the controlled synthesis of high-performance nanomaterials from industrial waste. This method enables the facile and large-scale production of functional, high-aspect-ratio nanowires, thereby contributing to the improvement of waste Si powder reutilization. Based on this study, it is expected that scaling up the synthesis process for higher efficiency will be the next key step. By adopting pulsed lasers or line-shaped laser beams, it should be possible to significantly increase the material yield beyond the current milligram scale. This would enable more comprehensive electrochemical assessments, including long-term cycling tests of several hundred cycles, which are crucial for real-world applications of these nanomaterials as advanced anode materials. These approaches also offer a sustainable route for the development of advanced energy storage materials.

CRediT authorship contribution statement

Kanon Minami: Writing – original draft, Visualization, Validation, Methodology, Investigation, Formal analysis, Data curation, Conceptualization. **Kentaro Shimazu:** Writing – original draft, Visualization, Validation, Investigation, Formal analysis, Data curation. **Yoshiyuki Hattori:** Writing – review & editing, Supervision, Resources, Project administration, Methodology, Investigation, Conceptualization. **Jiwang Yan:** Writing – review & editing, Supervision, Resources, Project administration, Methodology, Funding acquisition, Conceptualization.

Declaration of competing interest

The authors declare that they have no known competing financial interests or personal relationships that could have appeared to influence the work reported in this paper.

Acknowledgements

The authors would like to thank Dr. Kunimitsu Takahashi and Mr. Akihito Kawai of DISCO Corporation for their valuable suggestions and technical supports. This work was supported by the Japan Society for the Promotion of Science, Grant-in-Aid for Exploratory Research (project number 21K18681).

Data availability

No data was used for the research described in the article.

References

[1] M. Mottaghi, A. Kulkarni, J.M. Pearce, Recycling silicon photovoltaic cells into silicon anodes for Li-ion batteries using 3D printing, RSC Sustainability (2025), https://doi.org/10.1039/d4su00808a.
[2] C. Li, J. Wang, X. Wang, Z. Chen, R. Zhan, X. Duan, X. Liu, K. Cheng, Z. Cai, L. Wang, Y. Sun, Regulating the mechano-electrochemistry of graphite-silicon hybrid anode through layered electrode structure design, Journal of Energy Chemistry 104 (2025) 176–184, https://doi.org/10.1016/j.jechem.2024.12.048.
[3] X.Y. Zhang, W.L. Song, Z. Liu, H. Sen Chen, T. Li, Y. Wei, D.N. Fang, Geometric design of micron-sized crystalline silicon anodes through: in situ observation of deformation and fracture behaviors, J. Mater. Chem. A Mater. 5 (2017) 12793–12802, https://doi.org/10.1039/c7ta02527k.
[4] C.K. Chan, H. Peng, G. Liu, K. Mcllwrath, X.F. Zhang, R.A. Huggins, Y. Cui, High-performance lithium battery anodes using silicon nanowires, Nat. Nanotechnol. 3 (2008) 31–35, https://doi.org/10.1038/nnano.2007.411.
[5] J. Sourice, A. Quinsac, Y. Leconte, O. Sublemontier, W. Porcher, C. Haon, A. Bordes, E. De Vito, A. Boulineau, S. Jouanneau Si Larbi, N. Herlin-Boime, C. Reynaud, One-step synthesis of Si@C nanoparticles by laser pyrolysis: High-capacity anode material for lithium-ion batteries, ACS Appl Mater Interfaces 7 (2015) 6637–6644. https://doi.org/10.1021/am5089742.
[6] C. Qi, S. Li, Z. Yang, Z. Xiao, L. Zhao, F. Yang, G. Ning, X. Ma, C. Wang, J. Xu, J. Gao, Suitable thickness of carbon coating layers for silicon anode, Carbon N Y 186 (2022) 530–538, https://doi.org/10.1016/j.carbon.2021.10.062.
[7] H. Li, Q. Chen, L. Feng, Y. Zou, X. Gong, Z. Wang, J. Liu, Vapor-phase conversion of waste silicon powders to silicon nanowires for ultrahigh and ultra-stable energy storage performance, Journal of Energy Chemistry 102 (2025) 27–36, https://doi.org/10.1016/j.jechem.2024.10.039.
[8] P. Zhou, P. Xiao, F. Chu, W. Chen, Y. Li, F. Wu, Constructing Si/6H-SiC heterostructure as a high-performance anode for boosting lithium-ion storage, ACS Appl. Mater. Interfaces 16 (2024) 30088–30096, https://doi.org/10.1021/acsami.4c04312.
[9] T. Sri Devi Kumari, D. Jeyakumar, T. Prem Kumar, Nano silicon carbide: a new lithium-insertion anode material on the horizon, RSC Adv. 3 (2013) 15028–15034, https://doi.org/10.1039/c3ra40798e.
[10] H. Zhang, H. Xu, Nanocrystalline silicon carbide thin film electrodes for lithium-ion batteries, Solid State Ion. 263 (2014) 23–26, https://doi.org/10.1016/j.ssi.2014.04.020.
[11] H. Chen, Y. Hua, N. Luo, X. He, Y. Li, Y. Zhang, W. Chen, S. Huang, Lithiation abilities of SiC Bulks and surfaces: a first-principles study, J. Phys. Chem. C 124 (2020) 7031–7038, https://doi.org/10.1021/acs.jpcc.0c00103.
[12] Z. Wang, Z. Lei, R. Hong, M. Li, X. He, Plasma-enhanced synthesis of nitrogen-doped silicon carbide nanopowders in a fluidized-bed reactor for lithium-ion battery anodes, Chem. Eng. J. 514 (2025), https://doi.org/10.1016/j.cej.2025.163086.
[13] I. Shtepliuk, M. Vagin, Z. Khan, A.A. Zakharov, T. Iakimov, F. Giannazzo, I. G. Ivanov, R. Yakimova, Understanding of the electrochemical behavior of lithium at bilayer-patched epitaxial graphene/4H-SiC, Nanomaterials 12 (2022), https://doi.org/10.3390/nano12132229.
[14] H. Li, H. Yu, X. Zhang, G. Guo, J. Hu, A. Dong, D. Yang, Bowl-like 3C-SiC nanoshells encapsulated in hollow graphitic carbon spheres for high-rate lithium-ion batteries, Chem. Mater. 28 (2016) 1179–1186, https://doi.org/10.1021/acs.chemmater.5b04750.
[15] X. Li, L. Yuan, M. Li, R. Ji, Z. Han, S. Yu, K. Tang, Ag-doped hollow ZIFs-derived Si@C composite based on waste silicon for lithium-ion battery anodes, J. Am. Ceram. Soc. 108 (2025), https://doi.org/10.1111/jace.20568.
[16] H. Ji, Z. Han, X. Li, X. Xu, S. Yu, L. Yuan, M. Li, R. Ji, K. Tang, Synthesis of MWCNT-Si@Ag@CN composite with improved lithium storage performance from photovoltaic kerf loss Si waste, Ionics (Kiel) 31 (2025) 5465–5477, https://doi.org/10.1007/s11581-025-06323-z.
[17] K. Momoki, T. Manabe, L. Li, J. Yan, Silicon nanoparticle generation and deposition on glass from waste silicon powder by nanosecond pulsed laser irradiation, Mater. Sci. Semicond. Process. 111 (2020) 104998, https://doi.org/10.1016/j.mssp.2020.104998.
[18] K. Minami, K. Kobinata, J. Yan, Generation of Si@C/SiC@C core–shell nanoparticles by laser irradiation of silicon grinding waste, Nano Select (2022) 1–9, https://doi.org/10.1002/nano.202200001.
[19] K. Minami, K. Kobinata, J. Yan, Multilayer graphene-coated silicon carbide nanowire formation under defocused laser irradiation, Nanomanuf. Metrol. 6 (2023), https://doi.org/10.1007/s41871-023-00203-8.
[20] J.P. Moening, D.G. Georgiev, Formation of conical silicon tips with nanoscale sharpness by localized laser irradiation, J. Appl. Phys. 107 (2010), https://doi.org/10.1063/1.3273489.
[21] X. Li, Z. Yang, J. Wu, W. Wei, Y. Qiu, S. Jia, A. Qiu, Spatial confinement in laser-induced breakdown spectroscopy, J. Phys. D Appl. Phys. 50 (2017), https://doi.org/10.1088/1361-6463/50/1/015203.
[22] D. Zhang, A. Chen, X. Wang, Y. Wang, L. Sui, D. Ke, S. Li, Y. Jiang, M. Jin, Influence of the distance between target surface and focal point on the expansion dynamics of a laser-induced silicon plasma with spatial confinement, Spectrochim. Acta Part B At Spectrosc. 143 (2018) 71–77, https://doi.org/10.1016/j.sab.2018.02.017.

[23] W. Xu, A. Chen, Q. Wang, D. Zhang, S. Li, Y. Jiang, X. Gao, M. Jin, Characteristics of laser-induced aluminum plasma plumes after increasing sample temperature and spatial confinement, J. Anal. At. Spectrom 34 (2019) 2288–2294, https://doi.org/10.1039/c9ja00229d.
[24] X. Gao, L. Liu, C. Song, J. Lin, The role of spatial confinement on nanosecond YAG laser-induced Cu plasma, J. Phys. D Appl. Phys. 48 (2015), https://doi.org/10.1088/0022-3727/48/17/175205.
[25] A. Pendashteh, R. Tomey, J.J. Vilatela, Nanotextile 100% Si Anodes for the next generation energy-dense Li-ion batteries, Adv. Energy Mater. 14 (2024) 1–13, https://doi.org/10.1002/aenm.202304018.
[26] X.K. Yang, F.L. Zhang, W.T. Wu, Y. Tang, J. Yan, Y.L. Liu, C. Amatore, W.H. Huang, Quantitative Nano-amperometric measurement of intravesicular glutamate content and its sub-quantal release by living neurons, Angew. Chem. – Int. Ed. 60 (2021) 15803–15808, https://doi.org/10.1002/anie.202100882.
[27] X.W. Zhang, Q.F. Qiu, H. Jiang, F.L. Zhang, Y.L. Liu, C. Amatore, W.H. Huang, Real-time intracellular measurements of ROS and RNS in living cells with single core–shell nanowire electrodes, Angew. Chem. – Int. Ed. 56 (2017) 12997–13000, https://doi.org/10.1002/anie.201707187.
[28] F. Kokai, S. Inoue, H. Hidaka, K. Uchiyama, Y. Takahashi, A. Koshio, Catalyst-free growth of amorphous silicon nanowires by laser ablation, Appl. Phys. A Mater. Sci. Process. 112 (2013) 1–7, https://doi.org/10.1007/s00339-012-7169-y.
[29] K. Momoki, K. Takahashi, K. Kobinata, Y. Kobayashi, A. Kawai, J. Yan, Generating silicon nanofiber clusters from grinding sludge by millisecond pulsed laser irradiation, Nanomaterials 10 (2020) 7–9, https://doi.org/10.3390/nano10040812.
[30] K.M. Lv, J. Yang, K.Y. Niu, H.L. Wang, J. Sun, X.W. Du, Synthesis of Si-C nanostructures by laser ablation of silicon target in n-heptane vapor, Mater. Lett. 63 (2009) 2492–2494, https://doi.org/10.1016/j.matlet.2009.08.049.
[31] G.Z. Yang, H. Cui, Y. Sun, L. Gong, J. Chen, D. Jiang, C.X. Wang, Simple catalyst-free method to the synthesis of β-SiC nanowires and their field emission properties, J. Phys. Chem. C 113 (2009) 15969–15973, https://doi.org/10.1021/jp906167s.
[32] J. Wei, K. Li, J. Chen, H. Yuan, Synthesis of centimeter-scale ultra-long SiC nanowires by simple catalyst-free chemical vapor deposition, J. Cryst. Growth 335 (2011) 160–164, https://doi.org/10.1016/j.jcrysgro.2011.09.021.
[33] H. Huang, J.T. Fox, F.S. Cannon, S. Komarneni, In situ growth of silicon carbide nanowires from anthracite surfaces, Ceram. Int. 37 (2011) 1063–1072, https://doi.org/10.1016/j.ceramint.2010.11.022.
[34] K. Kao, M. Jiang, L. Ding, W. Lin, J. Chen, Catalytic synthesis of SiC nanowires in an open system, J. Am. Ceram. Soc. 102 (2019) 3070–3075, https://doi.org/10.1111/jace.16299.
[35] L. Hu, Y. Zou, C.H. Li, J.A. Liu, Y.S. Shi, Preparation of SiC nanowires on graphite paper with silicon powder, Mater. Lett. 269 (2020) 127444, https://doi.org/10.1016/j.matlet.2020.127444.
[36] S.Y. Oh, H. Imagawa, H. Itahara, Si-based nanocomposites derived from layered CaSi2: Influence of synthesis conditions on the composition and anode performance in Li ion batteries, J. Mater. Chem. A Mater. 2 (2014) 12501–12506, https://doi.org/10.1039/c4ta01318b.
[37] Z. Guo, Z. Liu, Y. An, C. Lu, C. Li, Y. Xu, L. Xie, X. Sun, X. Zhang, K. Wang, Y. Ma, Mitigating polarization effects in lithium-ion battery capacitors through conductive network enhancement, J. Energy Storage 127 (2025), https://doi.org/10.1016/j.est.2025.117106.